Biophysical Journal, Volume *111*

Supplemental Information

Mechanical Regulation of Three-Dimensional Epithelial Fold Pattern Formation in the Mouse Oviduct

Hiroshi Koyama, Dongbo Shi, Makoto Suzuki, Naoto Ueno, Tadashi Uemura, and Toshihiko Fujimori

Contents

Measurement of C-Epi/SM and L-Epi/SM ratios

The images of the longitudinally-opened oviducts were originated from our previous report (1). The samples were strained by Texas Red-X phalloidin (dilution rate = 1:100; Molecular Probes, Catalog #T7471).

The cross-sections of the oviducts were prepared as follows. The oviducts were fixed by 4% PFA (paraformaldehyde) in Ca^{2+}, Mg^{2+}-free phosphate-buffered saline (PBS) for overnight at 4 °C. The fixative was replaced by PBS and gradually up to 18% sucrose in PBS. Then the oviducts were embedded in Optimal Cutting Temperature (O.C.T.) compound (Sakura Finetek Japan, Japan), frozen in liquid nitrogen, and sectioned (5-10 μm) on a cryostat (Microm HM-500M; Carl Zeiss, Germany). The cryosections were rinsed with PBS and washed with 0.1% Triton X-100 in PBS for 20min. The samples were blocked with Blocking One (Nacalai Tesque, Japan) at 4°C overnight. After three washes with 0.01% Triton X-100 in PBS for 10min, the samples were incubated with Hoechst 33258 (1:1,000,000; Molecular Probes) and Texas Red-X phalloidin (1:100) in Blocking One at RT (room temperature) for 1-2 hour. After three-times washes with 0.1% Triton X-100 in PBS for 10min, the samples were mounted in Fluoromount-G (SouthernBiotech, U.S.A.). The fluorescent images were taken using a Nikon A1 confocal microscope (Nikon, Japan).

In the measurement of the C-Epi/SM ratio, an epithelium and a smooth muscle layer in a cross-section, were manually traced and their lengths were measured by using the ImageJ software (http://imagej.nih.gov/ij/). The epithelium was observed as a single continuous surface or sometimes as several segmented surfaces in a cross-section especially in the mutants (Fig.1E-ii). The lengths of the several segmented surfaces were included for the measurement of the C-Epi/SM ratio in Figure 1F.

In the rough estimation of the L-Epi/SM ratio, curvilinear fold length and the linear distance between two positions on a fold were measured in the longitudinally-opened oviducts. The rationale is described as follows (Fig.S2A). The linear distance between two positions (set of two asterisks) on a fold that were almost aligned along the longitudinal (*L*) direction is equal to the longitudinal length of the smooth muscle layer (SM_L) (left top and bottom panels). In the top two panels, the fold length between the two positions is equal not only to the longitudinal length of the epithelium (Epi_L) but also to that of the smooth muscle layer (SM_L). Therefore, the L-Epi/SM ratio becomes 1.0 ($=Epi_L/SM_L$). In the bottom two panels, the curvilinear fold length between the two positions may be roughly equivalent to the longitudinal length of the epithelium (Epi_L). Therefore, the L-Epi/SM ratio is estimated to be larger than 1.0 ($=Epi_L/SM_L$). In the calculation, first, we arbitrarily selected two positions that were

almost aligned along the longitudinal direction on the same fold. Due to the complex geometries of the folds especially in the Celsr1 mutant mice, we chose only relatively long continuous folds to be measured. Then, the two positions were manually connected along the fold or linearly. Finally, the two lengths were measured. The tracing and measurement were performed by using the ImageJ software.

Mathematical model of fold pattern formation

Parameter values used in simulations

R_{cs} was 0.5 D, and the ratio of R_{th}^{0} to R_{cs} was determined to be almost consistent with that of the thickness of the epithelia to the radius of the smooth muscle layers observed *in vivo*. E was fixed, and used to normalize other parameters. The values of K_{th} and K_{cs} had essentially no effect on the fold morphology when they were set to be large enough. Both the values of R_{th}^{0} and B affected the number of the folds. The number of the folds was negatively correlated with the values of R_{th}^{0} and B (Fig.S3C). The value of R_{th}^{0} was determined from the thickness of the epithelia observed *in vivo* as described above. The value of B was tuned so as to generate ~20 folds, consistent with the *in vivo* situation, but the value was almost physically reasonable (SI text, Comparison of epithelial

mechanical parameters with realistic values). E_L and E_C were set to be the same value as E, and B_L and B_C were set to be the same value as B. To avoid collapse of the grid shapes, S_{sq} should be larger than B_L and B_C (10.0-fold in the general conditions). The parameter values used in each simulation condition are shown in Table S1.

Table S1. List of parameter values used in the mechanical simulations.

	L-nEpi/ SM	C-nEpi/ SM	E_L*	E_C*	B_L* #	B_C* #	S_{sq}* #	λ_L*	λ_C*	
#1	1.0	3.0	1.0	1.0	2.4	2.4	24.0	-	-	Fig.2B, 2C (top)
#2	1.2	3.0	1.0	1.0	2.4	2.4	24.0	-	-	Fig.2C (middle)
#3	1.5	3.0	1.0	1.0	2.4	2.4	24.0	-	-	Fig.2C (bottom), S2F
#4	1.2	3.0	1.0	1.0	2.4	2.4	24.0	0.1	-	Fig.3A (top)
#5	1.2	3.0	1.0	1.0	2.4	2.4	24.0	0.2	-	Fig.3A (middle)
#6	1.2	3.0	1.0	1.0	2.4	2.4	24.0	0.33	-	Fig.3A (bottom)
#7	4.0	1.0	1.0	1.0	2.4	2.4	24.0	-	-	Fig.6A
#8	2.0	1.0	1.0	1.0	2.4	2.4	24.0	-	-	Fig.6B
#9	1.0	1.0	1.0	1.0	2.4	2.4	24.0	-	-	Fig.6C
#10	3.0	1.5	1.0	1.0	2.4	2.4	24.0	-	-	Fig.6D
#11	2.0	1.5	1.0	1.0	2.4	2.4	24.0	-	-	Fig.6E
#12	1.5	1.5	1.0	1.0	2.4	2.4	24.0	-	-	Fig.6F
#13	3.0	2.0	1.0	1.0	2.4	2.4	24.0	-	-	Fig.6G
#14	2.0	2.0	1.0	1.0	2.4	2.4	24.0	-	-	Fig.6H
#15	1.5	2.0	1.0	1.0	2.4	2.4	24.0	-	-	Fig.6I
#16	3.0	3.0	1.0	1.0	2.4	2.4	24.0	-	-	Fig.6J
#17	2.0	3.0	1.0	1.0	2.4	2.4	24.0	-	-	Fig.6K

#18	0.83	1.5	1.0	1.0	2.4	2.4	24.0	-	-	Fig.6M
#19	0.83	3.0	1.0	1.0	2.4	2.4	24.0	-	-	Fig.6N
#20	1.5	1.5	1.0	1.0	2.4	2.4	24.0	-	-	Fig.6O
#21	1.2	1.5	1.0	1.0	2.4	2.4	24.0	-	-	Fig.6P
#22	1.5	3.0	1.0	1.0	2.4	2.4	24.0	-	-	Fig.6Q
#23	1.2	3.0	1.0	1.0	2.4	2.4	24.0	-	-	Fig.6R
#24	1.2	3.0	1.0	1.0	0.24	0.24	24.0	-	-	Fig.S4A (first)
#25	1.2	3.0	1.0	1.0	0.72	0.72	24.0	-	-	Fig.S4A (second)
#26	1.2	3.0	1.0	1.0	12.0	12.0	24.0	-	-	Fig.S4A (third)
#27	1.2	3.0	1.0	1.0	72.0	72.0	24.0	-	-	Fig.S4A (fourth)
#28	1.2	3.0	1.0	1.0	2.4	2.4	2.4	-	-	Fig.S4B (first)
#29	1.2	3.0	1.0	1.0	2.4	2.4	8.0	-	-	Fig.S4B (second)
#30	1.2	3.0	1.0	1.0	2.4	2.4	72.0	-	-	Fig.S4B (third)
#31	1.2	3.0	1.0	1.0	2.4	2.4	240.0	-	-	Fig.S4B (fourth)
#32	1.2	3.0	0.1	0.1	2.4	2.4	24.0	-	-	Fig.S4C (first)
#33	1.2	3.0	0.33	0.33	2.4	2.4	24.0	-	-	Fig.S4C (second)
#34	1.2	3.0	3.0	3.0	2.4	2.4	24.0	-	-	Fig.S4C (third)
#35	1.2	3.0	10.0	10.0	2.4	2.4	24.0	-	-	Fig.S4C (fourth)
#36	1.0	3.0	1.0	1.0	2.4	2.4	24.0	-0.1	-	Fig.S4D (top)
#37	1.0	3.0	1.0	1.0	2.4	2.4	24.0	-0.2	-	Fig.S4D (bottom)
#38	1.2	3.0	1.0	1.0	2.4	2.4	24.0	-	0.1	Fig.S4E (left top)
#39	1.2	3.0	1.0	1.0	2.4	2.4	24.0	-	0.33	Fig.S4E (left middle)
#40	1.2	3.0	1.0	1.0	2.4	2.4	24.0	-	1.0	Fig.S4E (left bottom)
#41	1.0	3.0	1.0	1.0	2.4	2.4	24.0	-	-0.1	Fig.S4E (right top)
#42	1.0	3.0	1.0	1.0	2.4	2.4	24.0	-	-0.2	Fig.S4E (right bottom)

: $\times 10^{-5}$. B^* was 2.4×10^{-5}. K_{cs}^* and K_{th}^* were fixed as 333.3 and 200.0, respectively.

$R_{th}^{0}{}^*$ was 0.06. E is 3.0, D is 100, and μ is 1.0.

Table S2. Other parameter values used in Figure 6.

	Increase in the natural length of the elastic spring (fold)	Change in the longitudinal length of the surrounding constraint (fold)	*i*	*j*	
#7	1.0	0.25	133	400	Fig.6A
#8	1.2	0.5	133	200	Fig.6B
#9	1.0	1.0	133	150	Fig.6C
#10	1.5	0.5	267	350	Fig.6D
#11	1.5	0.75	267	200	Fig.6E
#12	1.5	1.0	200	200	Fig.6F
#13	2.0	0.67	267	350	Fig.6G
#14	2.0	1.0	267	200	Fig.6H
#15	2.0	1.33	267	200	Fig.6I
#16	3.0	1.0	400	200	Fig.6J
#17	3.0	1.5	400	200	Fig.6K
#18	3.0	3.6	200	100	Fig.6M
#19	1.5	1.8	400	100	Fig.6N
#20	1.0	0.556	200	100	Fig.6O
#21	1.0	0.694	200	100	Fig.6P
#22	1.0	0.556	400	100	Fig.6Q
#23	1.0	0.694	400	100	Fig.6R

The numbers (#7-23) corresponds to those in Table S1.

Calculation of epithelial tension in simulations

An epithelial tension in the simulations was defined as the force exerted on an edge of the grid, which was provided from both an elastic spring and a constrictive force on the edge (Fig.2E, and 3C). In Figure 2E and 3C, edges whose distances from the

surrounding constraint were more than 0.2*D* length were selected, because we focused on edges located around the top of folds. From the selected edges, edges whose angles to the longitudinal axis were 0 to $\pi/16$ radian or $7\pi/16$ to $\pi/2$ radian were analyzed for the calculation of longitudinal or C-plane epithelial tension, respectively. A dimensionless epithelial tension was obtained by normalizing the epithelial tension by *E*.

An index of epithelial tension was defined for each grid composed of four edges (Fig.2C, 3A, 6, S3Q, and S4). The longitudinal or C-plane components of the forces from the elastic springs and the constrictive forces of the four edges were averaged, and defined as the index of epithelial tension of the longitudinal or C-plane components, respectively. An index of dimensionless epithelial tensions was obtained by normalizing the index of epithelial tension by *E*. In Figure 2E and 3C, statistical tests were performed by using the two-sided and one-sided Student t tests, respectively.

Comparison of epithelial mechanical parameters with realistic values

We assumed that Young's modulus of the epithelium *Y* is 10^2-10^3[Pa], the diameter of the oviduct *D*=300[μm] (Fig.1E), and the thickness of the epithelium *H*=10[μm] (Fig.1E). The cross-sectional area of the epithelium *A* is ~$3\pi DH$. The node number in a

cross-section i is 400 (Fig.2A-v, i=400). We can write $Y=iE/A$, and thus, E was calculated to be 7.1-71[nN]. By using the value of E, the epithelial tension/E and λ_L* can be calculated. Epithelial tension derived from the former and the latter per unit length of the epithelium were calculated by using i and the length of the epithelium in a cross-section $3\pi D$. For example, the epithelial tension derived from λ_L per unit length of the epithelium is $=i\lambda_L/3\pi D$.

B* is $B/(E\,D^2)$ and B* was set to be 2.4×10^{-5}, thus, B was calculated to be $1.5\text{-}15\times10^{-11}$[nNm^2]. If we consider a cylindrical epithelium with the height l_0, the total bending energy along the circumferential direction is written as $u_{cv}\,(3\pi D\,l_0)$ by using B_{cv} or $i\,u_b$ by using B. These two terms should be equal, resulting in $B_{cv} = iB/(3\pi D)$. Consequently, B_{cv} was calculated to be $2.2\text{-}22\times10^{-6}$[nNm]. On the other hand, the bending modulus B_{cv} may be written as $B_{cv} = Y\,H^3/12(1-\nu^2)$, where ν is the Poisson ratio (4). If ν is 0.5, $B_{cv} = Y\,H^3/9$. According to this equation, B_{cv} is estimated to be $1.1\text{-}11\times10^{-5}$[nNm]. Therefore, the value of B_{cv} calculated from the value of B* used in our simulations is within the similar order of the above estimation, suggesting that the setting of the B* value is almost reasonable. In addition, even if B* is set to be five-times larger according to the above estimation (B* = 12×10^{-5}), the value will be within the parameter values used in Figure S4A.

Visualization of simulation results and count of branch number

Simulation results were visualized by the ParaView software (http://www.paraview.org/). Branches were manually counted on ParaView (Fig.S3R).

Laser ablation experiments

For laser ablation, three-week-old *Celsr1*$^{+/-}$*; R26-VMA (Venus fused with the actin binding domain of Moesin)* $^{+/-}$ (heterozygous) or *Celsr1*$^{-/-}$ *; R26-VMA*$^{+/-}$ (homozygous) mice were used. Oviducts were dissected and kept on ice until the measurement. For measurement, oviducts were longitudinally opened and placed on a glass-bottomed dish (P35G-1.5-10-C; MatTek, U.S.A.) filled with 1mM Ca^{2+} and Mg^{2+} phosphate buffered saline (PBS +). Confocal 512 × 512 images were acquired using a spinning disc confocal unit (CSU-X1; Yokogawa, Japan) with an EMCCD camera (iXon3; Andor) and a 488 nm laser on an inverted microscope (IX81; Olympus) with a 60× water immersion objective lens at room temperature and at 2.5 or 0.5 second intervals for estimation of epithelial tensions or cell boundary tensions, respectively. For a laser ablation experiment, a 365 nm laser with a dye (MP-27-365-DYE; Andor) was applied

to a single point, chosen manually, using MicroPoint Galvo (Andor). A 16 Hz pulse rate laser was irradiated the tissue twice at linearly aligned 11 points or at a single point for estimation of epithelial tensions or cell boundary tensions, respectively. The positional control was calibrated daily. Fresh samples were maintained during the experiment, as determined by monitoring ciliary movements. A fold forms a curved surface which may store bending energy. To reduce the influence of the bending energy on the results of the laser ablation experiment, we chose relatively flat surfaces.

For image analysis, images were aligned to correct for experimental drift using the ImageJ plugin StackReg (http://bigwww.epfl.ch/thevenaz/stackreg/)(5). Next, images were translocated and rotated so that the ablated point was the center of the image and the ablated cellular edge was horizontal. 300 × 300 pixel images were cropped and two images (before and after ablation) were selected for particle imaging velocimetry (PIV) analysis. PIV analysis was done using an ImageJ plugin (https://sites.google.com/site/qingzongtseng/piv)(6) with a parameter set (piv1=120, sw1=150, piv2=90, sw2=120, piv3=60, piv3=90, correlation=0.60). For the estimation of epithelial tensions, the components perpendicular to the ablation lines of each 4 arrows in the blue and green broken boxes were used (Fig. 4A-i). The averaged values of each 4 arrows were calculated. For the estimation of cell boundary tensions, four

vector values (W1–4) of the result around the ablation point were used to calculate the parallel displacement (= (W2x + W4x – W1x – W3x)/2) and the perpendicular displacement (= (W1y +W2y – W3y – W4y)/2) where Wi = (Wix, Wiy) for i = 1, 2, 3, 4. Regions corresponding to the vector are shown in Figure S5.

Mathematical analyses of epithelial tension using cell-arrays

In the calculation of epithelial tensions from *in silico* images, Voronoi diagrams were used (Fig.5B). A Voronoi diagram was drawn for ~400 seeds scattered in a 1.0 × 1.0 [A.U.] square region with 3 fixed seeds outside of the region. The randomly scattered 400 seeds generated the "random" diagram shown. To produce wild type– and *Celsr1*$^{-/-}$-like diagrams, we tried various scattering patterns and found that the following patterns successfully generated diagrams imitating both the distribution of the *in vivo* cell orientations and the longest/shortest diameter ratios. In the generation of the wild type–like diagrams, 36 × 11 = 396 seeds were uniformly distributed along the *C* and *L* directions, respectively. Then, fluctuations with maximum magnitudes of 0.5/36 [A.U.] and 0.5/11 were added for each seed along the *C* and *L* directions, respectively. Similarly, the *Celsr1*$^{-/-}$-like diagrams were generated from 20 × 20 = 400 uniformly

distributed seeds to which fluctuations with maximum magnitudes of 1.0/20 and 1.0/20 were added. The “rectangle” diagrams were generated from 31 × 13 = 403 seeds with 0.1/31 and 0.1/13 maximum fluctuation magnitudes. The “square” diagrams were generated from 20 × 20 with 0.5/20 and 0.5/20 maximum fluctuation magnitudes.

The epithelial tension of the Voronoi diagrams was calculated for 5 lines with lengths of 0.4 [A.U.], drawn at positions 0.3, 0.4, 0.5, 0.6, and 0.7 along the *L* direction which was perpendicular to the yellow lines (Fig.S6A-B, yellow lines). The epithelial tension perpendicular to each line was the sum of the tension produced from the cell boundaries crossing the line (Fig.5B-ii, bottom panel). The tension exerted by each cell boundary was assumed to be 1.0, and the *L* directed component of the tension was extracted to calculate the epithelial tension. The epithelial tension of a Voronoi diagram was defined as the average of the epithelial tension on the 5 lines.

In the estimation of epithelial tensions from *in vivo* images (Fig.5A), the number of cell boundaries crossing a laser irradiation line was counted and their angles to the line were measured. Under the assumption that the cell boundary tensions were uniform (=1.0), the sum of the components of the tensions perpendicular to the line was calculated.

Morphological analysis in oviduct swollen through ovulation

Super-ovulation was induced in female Slc;ICR mice as following. Three days before surgery, 5 U of pregnant mare's serum was injected at 5 pm, followed by another injection of 5 U of human chorionic gonadotropin at 5 p.m. of the day before surgery. Oviducts were dissected and put into PBS.

For video recording, movies were taken with a stereomicroscope connected with a digital camera (Nikon 1 J1; Nikon, Japan) under room temperature. For the morphological analyses, the oviducts were put into fixation solution (4% paraformaldehyde; PFA) and longitudinally opened soon after. Then, the oviducts were fixed further more at 4°C overnight in 4% PFA solution. The morphology of epithelial folds was visualized by immunohistochemistry, and 3D-reconstructed images were generated by multiple confocal microscopy images captured by Nikon A1 confocal microscope.

For the quantitative analyses, circumferential optical sections were made from 3D-reconstructed images in the NIS-elements software (Nikon, Japan) so that the section planes were perpendicular to the longitudinal axis. The interval distance between folds was measured at the base of each fold connecting the fold and the

circumferential tissue. The height of each fold was also measured. Note that we adopted the curvilinear length along the fold between the base and the tip as the index of the height, not the linear length nor the altitude.

Immunohistochemistry

Anti-E-cadherin hybridoma (ECCD-2) cell culture supernatant (dilution rate = 1:2) was a gift from M. Takeichi (7). Anti α-catenin α18 antibody (1:30) was a gift from A. Nagafuchi (8). The following reagents were purchased: anti Myh10 (1:100; Covance, Catalog #PRB-445P), anti Myh14 (1:100; Covance, Catalog #PRB-444P), Alexa Fluor–conjugated secondary antibodies (1:500; Molecular Probes), and Texas Red-X phalloidin (1:100; Molecular Probes, Catalog #T7471).

For whole-mount preparations, oviducts were dissected, opened longitudinally, and then the opened oviducts were fixed with 100% methanol at -20°C for 45 min and treated with acetone (-20°C for 5 min.). After treatment with 0.1% Triton X-100 in PBS, samples were blocked with Blocking One (Nacalai Tesque, Japan) at room temperature (RT), and incubated with primary antibodies in Blocking One at 4°C overnight. After washes with 0.1% Triton X-100 in PBS, the samples were incubated with fluorescently

labeled secondary antibodies at RT for 1 hr. After washes, the oviducts were mounted with their luminal side up in Fluoromount-G (SouthernBiotech, U.S.A.). The fluorescent images were taken using a Nikon A1 confocal microscope (Nikon, Japan).

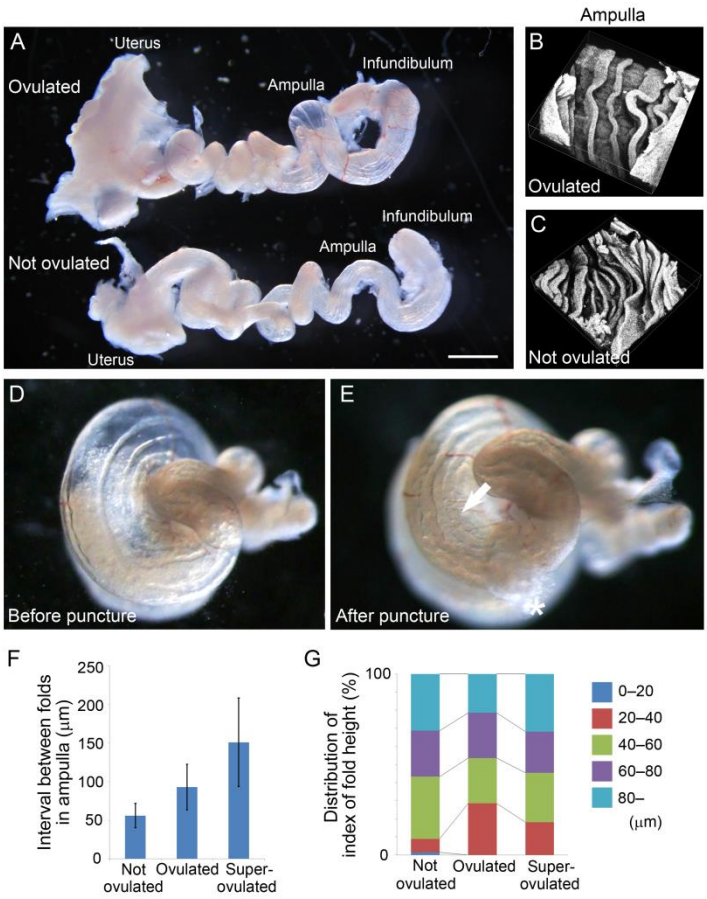

Fig. S1 Characteristics of the morphological change in epithelial folds induced through ovulation

A. An ovulated oviduct of a 9 weeks old female mouse (top) is compared to a non-ovulated oviduct (bottom). Note that the membranous tissues including the mesenteries connecting the oviducts were cut and removed for visualization. The ampulla was enlarged and filled with the ovulated oocytes (top). Scale bar, 1 mm.

B, C. Morphology of epithelial fold in the ampulla of the ovulated oviduct (B) and the non-ovulated oviduct (C). Oviducts were soaked into the fixation solution (4% paraformaldehyde) and longitudinally opened soon after. Cell contours were visualized by immunohistochemistry, and 3D reconstruction images were made from Z-stack confocal microscopy images. Outline indicates a 646 μm × 646 μm square.

D, E. Ampullar morphologies of a super-ovulated oviduct before (D) and after puncturing (E). Super-ovulation was induced by hormone treatment (SI text, Morphological analysis in oviduct swollen through ovulation). The asterisk indicates the place of the puncturing and the arrow indicates the winding epithelial folds after the puncturing. The interval distance between the folds became shorter after the puncturing. See also Movie S1.

F. Comparison of the average interval distance of the epithelial fold in the ampulla after ovulation and super-ovulation. Interval distances at the base of the epithelial folds were obtained from the 3D reconstructed images. 19 intervals from 4 oviducts (not ovulated), 16 intervals from 6 oviducts (ovulated), and 23 intervals from 5 oviducts (super-ovulated).

G. Distribution of the height of the ampullar fold after ovulation and super-ovulation. Note that the height indicates the curvilinear length along the epithelial fold between the

base and the tip of the fold in a circumferential optical section of the ampulla in 3D reconstructed images. 23 folds from 4 oviducts (not ovulated), 22 folds from 6 oviducts (ovulated), and 28 folds from 5 oviducts (super-ovulated). The 3D image sets in (F) were used for the analyses.

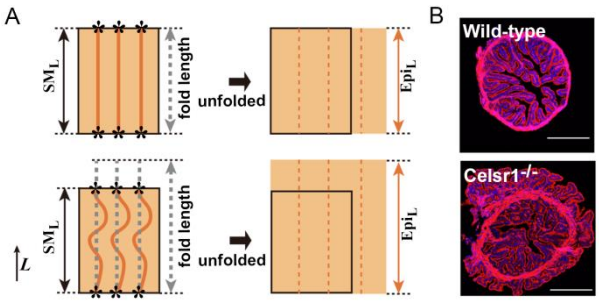

Fig. S2 Characterization of fold structures

A. Rationale of the rough estimation of L-Epi/SM ratio in Figure 1A. Cartoons of longitudinally-opened oviducts are shown with well-aligned folds (left top panel) and randomly-directed folds (left bottom panel). Cartoons of unfolded epithelia into flat sheets are shown (right two panels). Black rectangles: smooth muscle layers (SM). Orange rectangles: epithelia (Epi). Orange solid lines: epithelial folds. Set of two asterisks in a fold: two positions on a fold that are almost aligned along the longitudinal (*L*) direction. Orange broken line in right panels: original positions of folds before unfolded. Gray broken lines: corresponding to fold lengths. SM_L: longitudinal length of the smooth muscle layer. Epi_L: longitudinal length of the epithelium. The fold lengths may be roughly equivalent to Epi_L.

B. Other examples of the cross-section of the oviduct in Figure 1B.

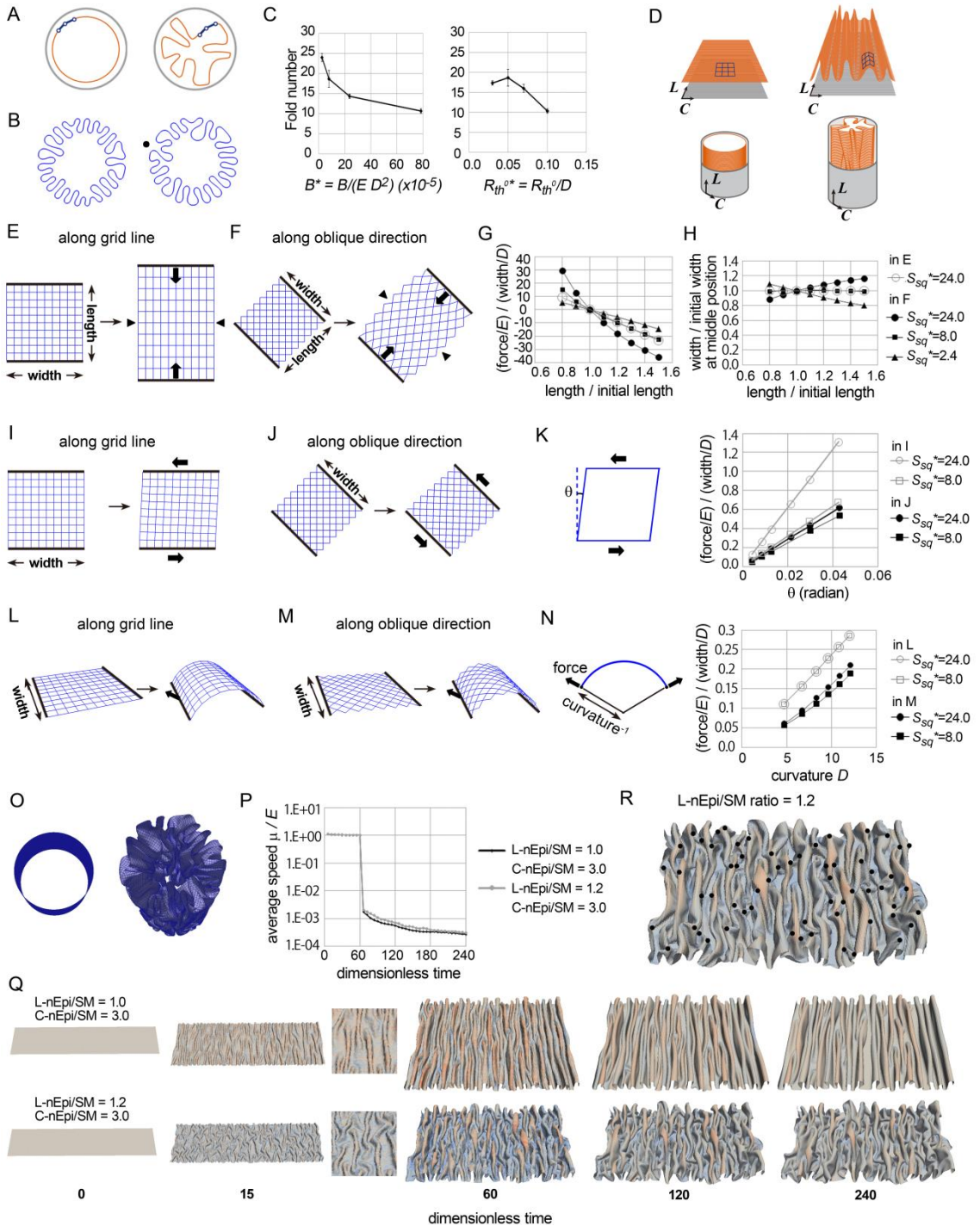

Fig. S3 Mathematical modeling and simulation

A. Schematic illustration of initial (left panel) and final states (right panel) in cross-sectional-simulations.

B. Two examples of simulation results of the cross-sectional-model. A radial branch is shown (closed circle). The elastic sheet is shown and the surrounding constraint is hidden.

C. Effect of bending elasticity B (left panel) and the thickness of the sheet R_{th}^{0} (right panel) on number of folds. These parameter values were determined as shown in SI text (Parameter values used in simulations).

D. Schematic illustration of initial (left panels) and final states (right panels) in 2D sheet-simulations embedded in 3D cylinder. Original views (bottom panels) and longitudinally-opened views (top panels) are shown.

E-H. Responses of the 2D sheet model to stretch and compression. The model composed of grids is shown by blue grids. Simulation results of stretch / compression along the grid lines (E) and along the direction oblique to the grid lines (F) are shown. The forces exerted by the sheet during the stretch / compression (bold arrows in E and F) are plotted against the ratio of the length to the initial length, where inward and outward forces are defined as minus and plus, respectively (G). Dimensionless values are shown. The widths at the middle positions of the sheets (arrowheads in E and F) are also plotted (H).

I-K. Responses of the 2D sheet model to shear deformation. The model composed of grids is shown by blue grids. Simulation results of shear along the grid lines (I) and along the direction oblique to the grid lines (J) are shown. A schematic illustration of shear and the deformation defined by θ are shown (K, left panel). The forces exerted by the sheet (bold arrows in I, J, and K, left panel) are plotted against θ (K, right panel). Dimensionless values are shown.

L-N. Responses of the 2D sheet model to bending deformation. The model composed of grids is shown by blue grids. Simulation results of bending along the grid lines (L) and along the direction oblique to the grid lines (M) are shown. A schematic illustration of bending and the deformation defined by curvatures are shown (N, left panel). The forces exerted by the sheet (bold arrows in L, M, and N, left panel) are plotted against curvatures (K, right panel). Dimensionless values are shown.

O. Simulation results at an initial (left panel) and final states (right panel).

P-Q. Convergences of simulations are evaluated. Dimensionless average speeds of nodes are plotted against dimensionless simulation time (P). Representative states of simulations are shown (Q). Enlarged views at dimensionless time = 15 are also shown.

R. An example of counting branch numbers. Black closed circles: branches. The image used is the same as Figure 2C, middle panel.

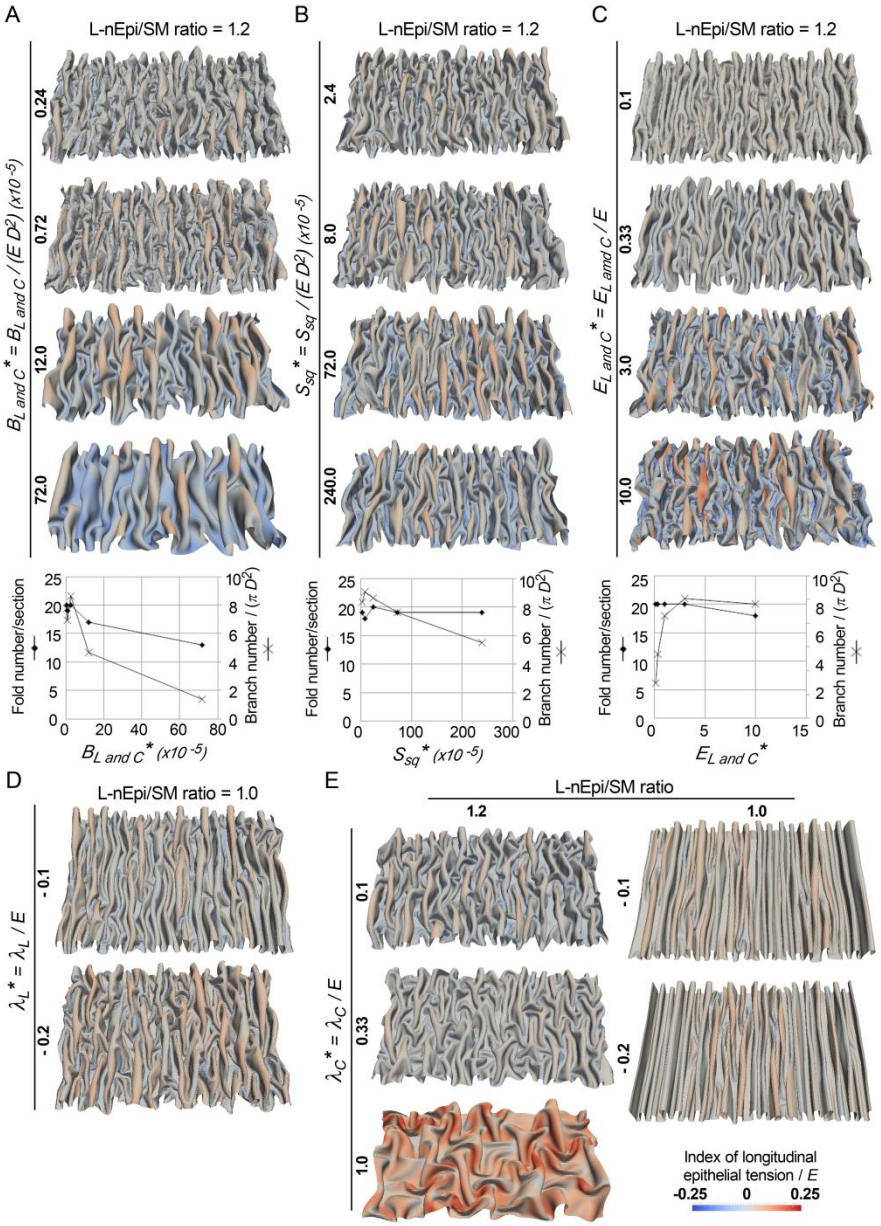

Fig. S4 Effect of various parameters on fold pattern formation

Effect of coefficients of bending springs, B_L and B_C (A), coefficient of bending springs for shear stress, S_{sq} (B), coefficients of elastic springs, E_L and E_C (C), longitudinal negative constrictive force λ_L (D), and circumferential constrictive force λ_C (E). Fold

numbers per a cross-section of the cylinder and branch numbers are shown for A-C. Index of dimensionless longitudinal epithelial tensions is shown by blue-red colors in all Figures. The longitudinal negative λ_L induced branching (D).

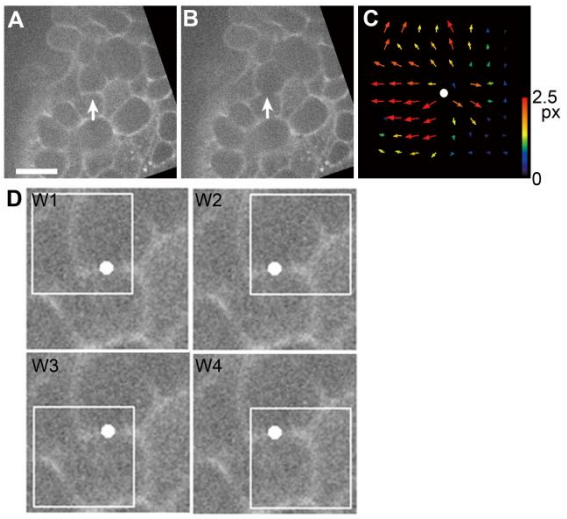

Fig. S5 Experimental procedures of PIV analysis after laser ablation on cell boundary

A. Before laser irradiation. White arrows: laser irradiation point. Scale bar, 10μm.

B. After laser irradiation. White arrows: laser irradiation point.

C. Result of PIV analysis. The colors and lengths of the arrows indicated the displacements (in pixels) of corresponding regions as represented by the scale. White close circle: laser irradiation point.

D. Calculations of the displacement along the direction parallel (P) or vertical (V) to the cell boundary. Magnified views around the ablation point in A are shown. The displacements at the regions W1-4 were combined to calculate the P or V displacements. Details are shown in SI text. White close circles: laser irradiation point.

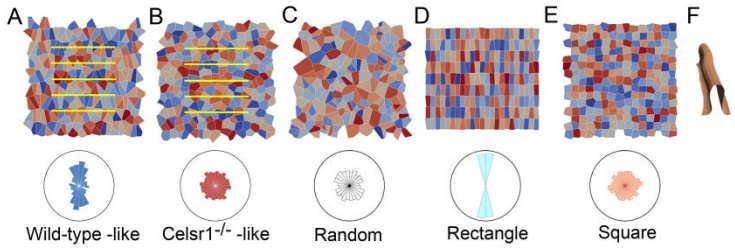

Fig. S6 Voronoi diagrams resembling in *vivo* situations

A-E. Whole views of the Voronoi diagrams in Figure 5B-i are shown with the distributions of major angles of the cells (rose diagrams). Yellow lines: the calculation positions. The rose diagrams in Figure 5B-ii are presented again.

F. A schematic illustration of a fold to identify the direction in A-E.

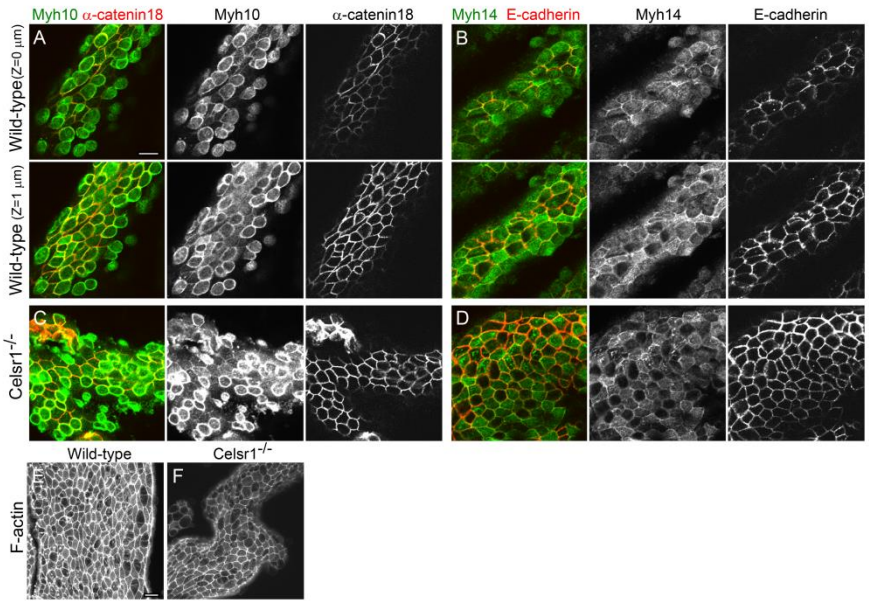

Fig. S7 Localization of marker proteins related to cellular mechanics

A–F. Localization of Myh10 (non-muscle myosin II-b), α-catenin (detected by α-18 antibodies), Myh14 (non-muscle myosin II-c), E-cadherin, and F-actin (detected by Phalloidin) in the oviduct epithelium of 3 weeks old wild type mice (A, B, E) and *Celsr1*$^{-/-}$ mutant mice (C, D, F). Confocal microscopy images (A–D) and maximum intensity projection images (E, F) are shown. In addition to the images focused around the top of the fold (A and B, Z=0 μm), the images with a focal plane 1 μm more basal to the former images are also shown (A and B, Z=1 μm). Scale bars, 10 μm. Note that Myh10 not only localized to the contour of apically-protruded cells (secretory cells) (Z=0 μm) strongly, but also localized to the contour of flat cells (ciliated cells) (Z=1 μm). α-18 antibodies are reported to recognize α-catenin under mechanically stressed-states (8).

Movie S1 Morphological change during the puncturing

Changes in ampullar morphologies of a super-ovulated oviduct during and after the puncturing. See also Figure S1. Time stamp indicates min:sec.

Supporting References

1. Shi, D., K. Komatsu, M. Hirao, Y. Toyooka, H. Koyama, F. Tissir, A.M. Goffinet, T. Uemura, and T. Fujimori. 2014. Celsr1 is required for the generation of polarity at multiple levels of the mouse oviduct. Development. 141: 4558–4568.
2. Shyer, A.E., T. Tallinen, N.L. Nerurkar, Z. Wei, E.S. Gil, D.L. Kaplan, C.J. Tabin, and L. Mahadevan. 2013. Villification: how the gut gets its villi. Science. 342: 212–8.
3. Ben Amar, M., and F. Jia. 2013. Anisotropic growth shapes intestinal tissues during embryogenesis. Proc. Natl. Acad. Sci. U. S. A. 110: 10525–30.
4. Hannezo, E., J. Prost, and J.F. Joanny. 2012. Mechanical instabilities of biological tubes. Phys. Rev. Lett. 109: 018101.
5. Thévenaz, P., U.E. Ruttimann, and M. Unser. 1998. A pyramid approach to subpixel registration based on intensity. IEEE Trans. Image Process. 7: 27–41.
6. Tseng, Q.Z., E. Duchemin-Pelletier, A. Deshiere, M. Balland, H. Guillou, O. Filhol, and M. Thery. 2012. Spatial organization of the extracellular matrix regulates cell-cell junction positioning. Proc. Natl. Acad. Sci. U. S. A. 109: 1506–1511.
7. Shirayoshi, Y., A. Nose, K. Iwasaki, and M. Takeichi. 1986. N-linked oligosaccharides are not involved in the function of a cell-cell binding glycoprotein E-cadherin. Cell Struct. Funct. 11: 245–252.
8. Yonemura, S., Y. Wada, T. Watanabe, A. Nagafuchi, and M. Shibata. 2010. alpha-Catenin as a tension transducer that induces adherens junction development. Nat. Cell Biol. 12: 533–542.